PNAS RESEARCH ARTICLE | CHEMISTRY

Long wavelength–emissive Ru(II) metallacycle–based photosensitizer assisting in vivo bacterial diagnosis and antibacterial treatment

Yuling Xu[a,1], Chonglu Li[a,1], Xin Ma[a,1], Wei Tuo[b], Le Tu[c], Xiaopeng Li[d], Yan Sun[b,e,2], Peter J. Stang[b,2], and Yao Sun[a,2]

Edited by Chad Mirkin, Northwestern University, Evanston, IL; received March 4, 2022; accepted June 23, 2022

Ruthenium (Ru) complexes are developed as latent emissive photosensitizers for cancer and pathogen photodiagnosis and therapy. Nevertheless, most existing Ru complexes are limited as photosensitizers in terms of short excitation and emission wavelengths. Herein, we present an emissive Ru(II) metallacycle (herein referred to as 1) that is excited by 808-nm laser and emits at a wavelength of ∼1,000 nm via coordination-driven self-assembly. Metallacycle 1 exhibits good optical penetration (∼7 mm) and satisfactory reactive oxygen species production properties. Furthermore, 1 shows broad-spectrum antibacterial activity (including against drug-resistant *Escherichia coli*) as well as low cytotoxicity to normal mammalian cells. In vivo studies reveal that 1 is employed in precise, second near-infrared biomedical window fluorescent imaging–guided, photo-triggered treatments in *Staphylococcus aureus*–infected mice models, with negligible side effects. This work thus broads the applications of supramolecular photosensitizers through the strategy of lengthening their wavelengths.

supramolecular coordination complexes | metallacycle | long-wavelength emissive

Bacterial infections are identified as the main causes of morbidity and mortality worldwide. This situation is further compounded by antibiotic resistance to antibacterial therapies (1, 2). To address drug resistance, antibacterial methods such as photosensitizers with a photodynamic therapy feature have been developed against bacterial infections (3–9). Metal-based photosensitizers with tunable photophysical and biological properties can further advance phototherapeutic efficiency to benefit antibacterial applications (10–13). However, the majority of current, metal-based photosensitizers are featured with short excitation and emission wavelengths (<700 nm) (14–18), which limits their efficiency in fluorescent imaging and photo-triggered treatments in deep biological tissue, thus serving as motivation to design and synthesize novel metal-based photosensitizers which have longer excitation and emission profiles.

Emissive supramolecular coordination complexes (SCCs) with well-tuned sizes, shapes, and outstanding photophysical features are developed through coordination-driven self-assembly for biomedicine (19–27). The properties including fluorescent and phototherapeutic performance of SCCs, in many instances, can be further tuned through imbedding appropriate molecular ligands (28–30). However, studies of metallacycles and metallacages in bacterial detection and antibacterial applications are still in their infancy (31–33) and, to our knowledge, only include very few in vivo cases (34). This could be due to the relatively short excitation and emission wavelengths (<700 nm) and inadequate photodynamic therapy outcome of current SCCs (35–38). We and other researchers have constructed the second near-infrared biomedical window (NIR-II; 1000 to 1700 nm) agents that showed deeper optical penetration, better spatiotemporal resolution, and higher phototherapeutic efficiency compared with the counterparts which are excited or emit in ultraviolet and visible ultraviolet light (280 to 700 nm) and the first near-infrared (700 to 900 nm) regions (39–47). Hence, extending the excitation and emission wavelengths of metallacycle-based photosensitizers is imperative for further biomedical application.

Considering the above statements, we developed a ruthenium (II) [Ru(II)] metallacycle (hereafter referred to as **1**), which emits at ∼1,000 nm through self-assembly of the donor–acceptor–donor scaffold NIR-II fluorescent ligand **2** with the dinuclear arene-Ru **3** (Scheme 1). The design that integrates NIR-II fluorophores and metal Ru(II) thereby contributes to some superiorities for in vivo bacterial imaging and killing, including excellent photostability, deep optical penetration, fluorescent imaging with high spatiotemporal resolution, and satisfactory photo-triggered treatments. Ru(II) metallacycle **1** shows a high efficacy and broad-spectrum in vitro antibacterial activity, which is likely due to **1**-mediated bacterial membrane damage. Complex **1**

Significance

Bacterial infection is the major risk to public health. Developing emissive metal–based photosensitizers against bacterial infections draws continued interest in biomedicine. The most important issue is extending the absorption and emission wavelengths of metal-based photosensitizers to ameliorate the efficiency of in vivo imaging and phototherapy. To address this, we rationally designed a long-wavelength–emissive ruthenium (II) metallacycle (herein referred to as **1**) that has superior optical penetration (∼7 mm) and satisfactory reactive oxygen species–generation performance. Complex **1** has promising broad-spectrum antibacterial activity and low toxicity to mammalian cells. Moreover, **1** enables high-performance, in vivo, fluorescent imaging-guided phototherapy of *Staphylococcus aureus*–infected mice, with ignorable adverse effects, thus demonstrating that **1** could be a good platform for pathogen phototheranostics.

Author contributions: Yan Sun, P.J.S., and Yao Sun designed research; Y.X., C.L., X.M., W.T., L.T., and X.L. performed research; P.J.S. contributed new reagents/analytic tools; and Yan Sun, P.J.S., and Yao Sun wrote the paper.

The authors declare no competing interest.

This article is a PNAS Direct Submission.

[1]Y.X., C.L., and X.M. contributed equally to this work.

[2]To whom correspondence may be addressed. Email: elaine.sun@utah.edu or stang@chem.utah.edu or sunyaogbasp@ccnu.edu.cn.

This article contains supporting information online at http://www.pnas.org/lookup/suppl/doi:10.1073/pnas.2209904119/-/DCSupplemental.

Published August 1, 2022.

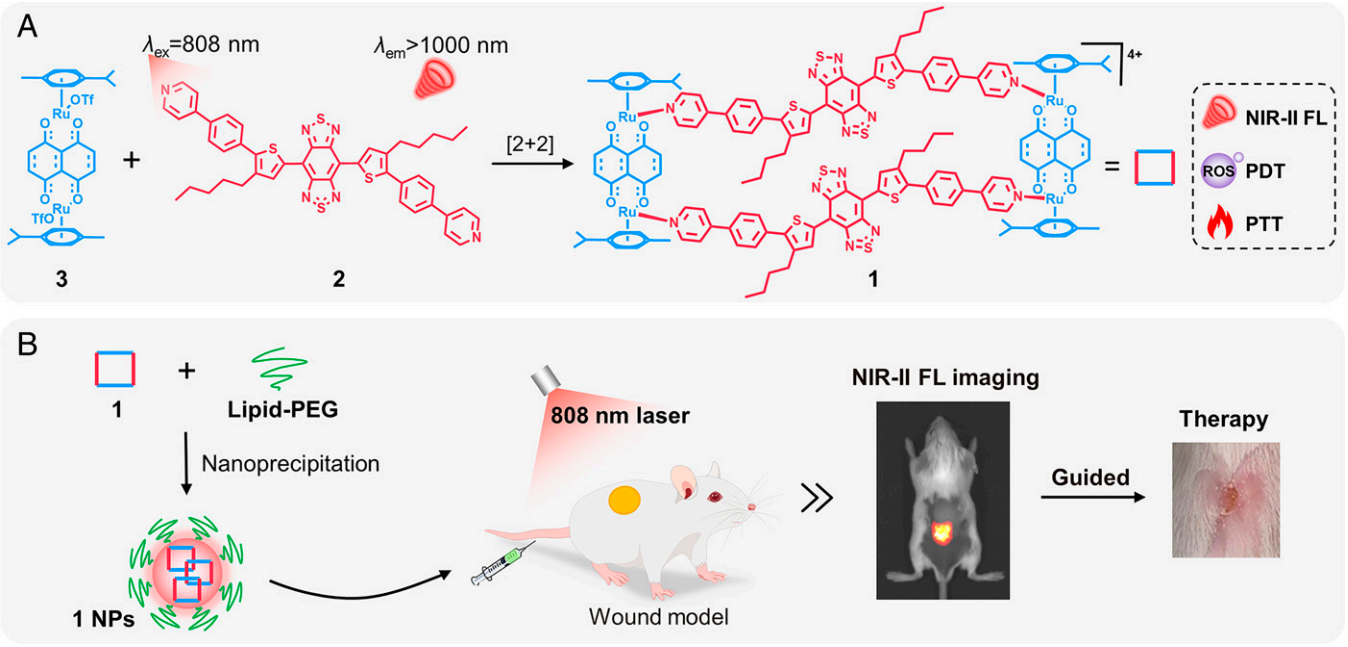

Scheme 1. Cartoon illustration of (*A*) metallacycle 1 and (*B*) NIR-II fluorescent imaging–guided efficient therapy of a *Staphylococcus aureus*–infected wound model using metallacycle 1. PEG, pegylated; PDT, photodynamic therapy; PTT, photothermal therapy.

affords high-contrast in vivo NIR-II fluorescent imaging of *Staphylococcus aureus* and then precise imaging-guided phototherapy of pathogen-infected mice, with ignorable side effects. Thus, we believe this work establishes a paradigm in supramolecular theranostic agents in bacterial infections with the possibility of tackling drug resistance.

Results and Discussion

Synthesis of Ru(II) Metallacycle 1. NIR-II fluorescent ligand **2** was designed based on the optimized donor–acceptor–donor scaffold with the phenylpyridine group as the Ru(II) coordination unit (*SI Appendix*, Section B) though molecular engineering. Ligand **2** was further confirmed and characterized (*SI Appendix* Figs. S1–S9 and Scheme 1).

Ru(II) metallacycle **1** was constructed through the [2 + 2] coordination-driven self-assembly of fluorescent ligand **2** and Ru(II) acceptor **3** (48) by stirring a 1:1 mixture in $CHCl_3$/MeOH for 24 h (Fig. 1*A* and *SI Appendix*, Section B). The formation of assembly **1** with a yield of 60% was fully characterized (*SI Appendix*, Figs. S10–S13). The proton of the pyridyl moiety (H_{2a}) of **1** displayed an upfield shift (from 8.64 to 8.37 ppm) compared with ligand **2.** Moreover, the peaks belonging to the *p*-cymene protons (H_{3b} and H_{3c}) also showed upfield shifts compared with those of the Ru(II) acceptor **3**, owing to the transference of electron density in the nitrogen atoms of pyridine to the electron-deficient Ru(II) after coordination-driven self-assembly (Fig. 1*B*). The $^{19}F\{^1H\}$ NMR spectrum of **1** showed one single peak (−79.062 ppm), which belongs to the triflate counter anions (*SI Appendix*, Fig. S11). Additionally, the two dimensional–rotating frame Overhauser-effect spectroscopy spectrum was characterized by cross peaks between the pyridyl protons from ligand and acceptor (*SI Appendix*, Fig. S12). Electrospray ionization time-of-flight mass spectrometry analysis exhibited two main peaks and confirmed the stoichiometry according to the formation of a rectangular metallacycle **1** (Fig. 1*C* and *SI Appendix*, Fig. S13), which included those corresponding to an intact entity with various charges consistent with the loss of OTf^- counterions (m/z = 1006.7979 for $[\mathbf{1}–3OTf]^{3+}$ and 718.1162 for $[\mathbf{1}–4OTf]^{4+}$). The peaks in the electrospray ionization time-of-flight mass spectrometry spectrum matched well with the theoretical patterns. Furthermore, we used Gaussian 09 software to perform the geometry optimizations of structure **1** (Fig. 1*D*). According to the optimized geometry, the distance between the centroids of ligand **2**, as well as the distance between the two Ru centers coordinated to ligand **2**, were 19.03 Å and 29.92 Å, respectively. These results supported the development of Ru(II) metallacycle **1**.

In Vitro Photophysical Properties of Ru(II) Metallacycle 1. The absorption and emission spectra of **1** were measured (*SI Appendix*, Figs. S14 and S15). Due to intraligand charge transfer, **1** showed a maximum absorption peak at ∼760 nm in *N*,*N*-dimethylformamide (DMF) (16). The maximum emission wavelength of **1** in DMF was ∼1,000 nm, located within the NIR-II biological window (Fig. 2*A*). The molar absorption coefficient (ε) and the relative quantum yield (Φ_F) of **1** in DMF were determined to be 33,300 M^{-1} cm^{-1} and 0.46%, respectively (*SI Appendix*, Table S1).

We further evaluated the stability of **1** under physiological conditions. The chemical stability of **1** was assessed through recording the absorption spectra in various solutions. As shown in Fig. 2*B* and *SI Appendix*, Figs. S16 and S17, **1** exhibited good stability under different pH conditions as well as both in phosphate-buffered saline and 10% fetal bovine serum. Complex **1** also possessed good photostability under continuous 808-nm laser irradiation (*SI Appendix*, Fig. S18). Then the optical penetration of **1** was evaluated in a tissue mimic using a commercial photosensitizer, $Ru(bpy)_3^{2+}$, as a control. Compared with the fluorescent signal of $Ru(bpy)_3^{2+}$, which essentially became almost invisible when the penetration depth was increased just to 1 mm, the signal of **1** was distinguished even the penetration depth increased to 7 mm. (Fig. 2*C*).

In Vitro Reactive Oxygen Species Generation and Photothermal Properties. We used a classic reactive oxygen species (ROS) indicator, 2′,7′-dichlorodihydrofluorescein diacetate (DCFH-DA), to evaluate the in vitro ROS production capability. The

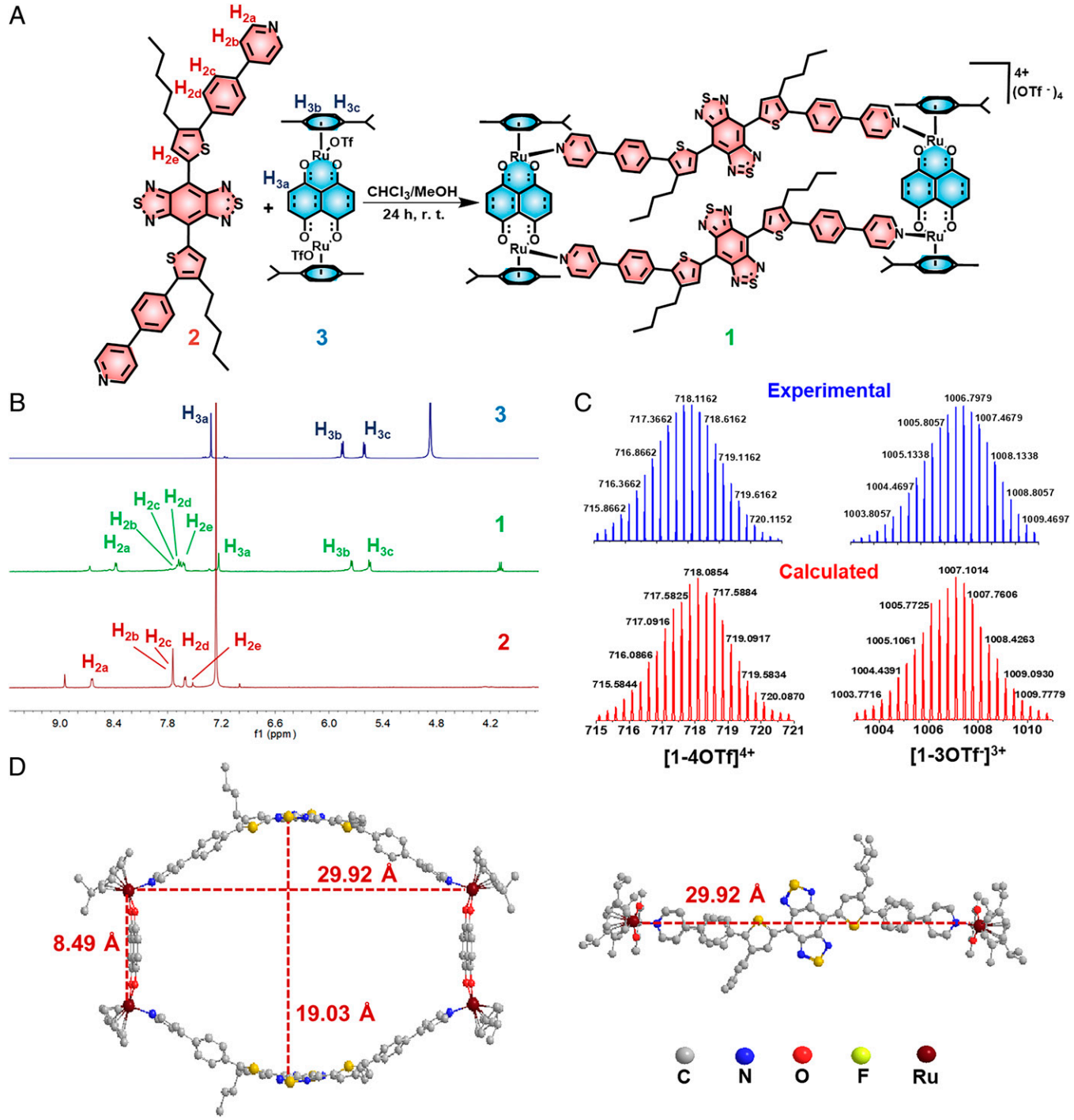

Fig. 1. Synthetic scheme, NMR/mass spectrometry (MS) characterization and theoretical calculation of **1**. (*A*) Self-assembly of **2** with **3** to obtain Ru(II) metallacycle **1**. (*B*) Partial ^{1}H NMR spectra of **3** (*Top*), **2** (*Bottom*) and **1** (*Middle*). (*C*) Experimental and calculated MS spectra of **1** (*Left*: [**1**-4OTf]$^{4+}$ charge state; *Right*: [**1**-3OTf]$^{3+}$ charge state). (*D*) The optimized structure of **1**. The hydrogen atoms in the structure are omitted for clarity. r.t., room temperature.

fluorescent intensity (540 nm) increased rapidly with incubated with **1** under continuous 808-nm irradiation (Fig. 2*D*). Moreover, compared with the ligand **2**, complex **1** exhibited nearly a 1.7-fold ROS generation increase (*SI Appendix*, Fig. S19). The improved ROS production could be attributed to the introduction of heavy-atom Ru into the metallacycle and the promotion of intersystem crossing (49). Besides, the Ru(II) acceptor **3** showed little ROS production under the same condition (*SI Appendix*, Fig. S20). This result indicated the high-efficiency ROS generation of **1**. We used commercially available ROS indicators to distinguish the ROS species generated by **1**. Hydroxyphenyl fluorescein and dihydrorhodamine 123 were utilized to detect the hydroxyl radical (•OH) and superoxide anion ($\bullet O_2^-$) generation, respectively. The fluorescent intensity changes of hydroxyphenyl fluorescein and dihydrorhodamine 123 both rapidly increased upon the irradiation time in the presence of **1**, indicating efficient •OH and $\bullet O_2^-$ generation (*SI Appendix*, Fig. S21). Moreover, the energy gap ($\triangle E_{st}$) of **1** was 0.42 eV, further indicating a high intersystem crossing rate for efficient ROS production (*SI Appendix*, Fig. S22).

The photothermal characteristics of **1** were then determined by measuring the temperature of a solution of **1**, and a significant

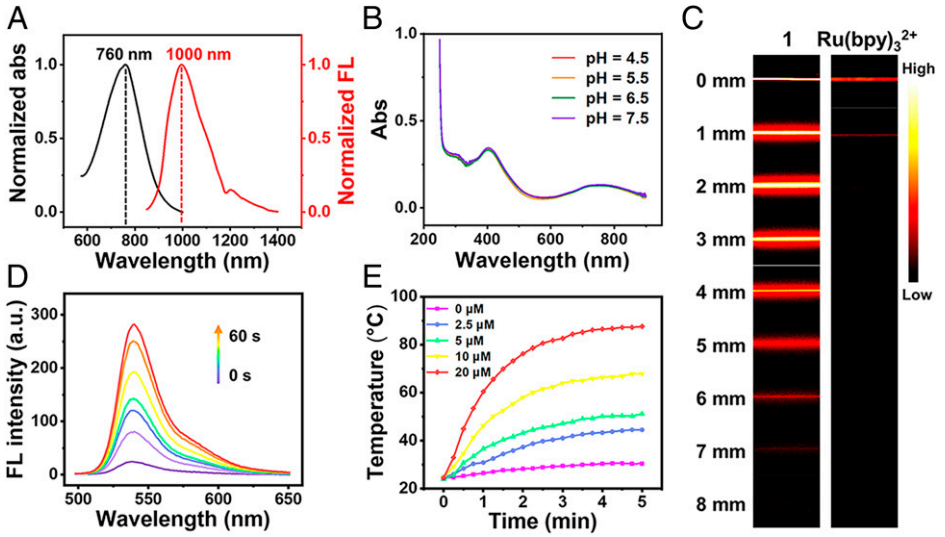

Fig. 2. In vitro photophysical features of **1**. (*A*) Normalized absorption/emission spectra (λ_{ex} = 808 nm) of **1** in DMF. (*B*) The solution stability tests of **1** in different pH conditions. (*C*) Fluorescent imaging of **1** and $Ru(bpy)_3^{2+}$ under different depths in 1% intralipid. (*D*) ROS generation of **1** (20 μM) under 808-nm laser irradiation (0.5 W cm^{-2}). (*E*) Temperature-change curves of **1** (0 to 20 μM) under 808-nm laser irradiation (0.8 W/cm^2). abs, absorption; a.u., arbitrary units; FL, fluorescence.

temperature increase was observed within a concentration range of 0 to 20 μM (Fig. 2*E*). As depicted in *SI Appendix*, Fig. S23, **1** exhibited higher photothermal conversion efficiency (39.0%) than indocyanine green (15.8%), the US Food and Drug Administration–approved fluorescent dye (50). Moreover, good photothermal stability of **1** was discovered without obvious temperature decline in heating and natural cooling tests (*SI Appendix*, Fig. S24).

In Vitro Antimicrobial Activity. Antibacterial activity was measured through recording the optical densities at 600 nm and taking photographs of the agar plates of bacteria after different treatments (*SI Appendix*, Section A). Gram-positive (G+) bacteria (*Staphylococcus aureus*) and *Streptococcus pneumoniae*) and Gram-negative (G–) bacteria (*Escherichia coli* and kanamycin-resistant *E. coli*) were selected to test the antibacterial activity of **1**. As shown in Fig. 3 and *SI Appendix*, Fig. S25 (*SI Appendix*, Section C), **1** showed a dose-dependent antibacterial activity against these four kinds of bacteria, including drug-resistant *E. coli*. Furthermore, **1**, with or without 808-nm laser irradiation (10 min), had better killing effect on G+ bacteria than G– bacteria. This antibacterial selectivity was likely due to the thicker and more complex cell-wall structure of G– bacteria (51). Moreover, **1** exhibited low cytotoxicity in normal cells (i.e., 16HBE cells), which indicated the good biocompatibility, specificity, and selectivity of the **1**-based photosensitizer in antibacterial applications (*SI Appendix*, Fig. S26). Furthermore, after incubation with **1** and further irradiation with the 808-nm laser, *Staphylococcus aureus* and *E. coli* exhibited enhanced green fluorescence when stained with DCFH-DA, indicating that ROS can be efficiently produced in bacteria (*SI Appendix*, Fig. S27).

In Vitro Bacteria Imaging. We incubated metallacycle **1** with *S. aureus* and *E. coli* to test the interactions with bacteria (*SI Appendix*, Section A). As shown in Fig. 4*A*, a strong NIR-II fluorescent signal was observed in bacteria after they were incubated with **1**. The average fluorescent intensity on *S. aureus* was nearly 2.3-fold as much as that on *E. coli* (Fig. 4*B*), which suggested higher uptake of **1** in *S. aureus* than in *E. coli*. The bacterial uptake of **1** was quantitatively analyzed through inductively coupled plasma mass spectrometry. The amount of metal Ru in *S. aureus* (131.5 ng/mg cells) was more than that in *E. coli* (47.2 ng/mg cells), matching well with fluorescent imaging results (Fig. 4*C*). In addition, scanning electron microscope characterization revealed that the combination of **1** and laser irradiation caused the bacterial cell wall to wrinkle and distort to varying degrees, thereby resulting in bacterial death (red arrows in Fig. 4*D*). Finally, the results of zeta potential demonstrated a reduced negative charge of bacteria after their binding with the positively charged metallacycle **1** (Fig. 4*E*).

In Vivo Bacteria Imaging and Antibacterial Assays. Furthermore, we prepared nanoparticles (NPs) with **1** by formulating 1,2-distearoyl-sn-glycero-3-phosphoethanolamine–methoxy polyethylene glycol 5000 (DSPE-mPEG5000) (*SI Appendix*, Section C). DSPE- mPEG5000 with ultralow cytotoxicity could

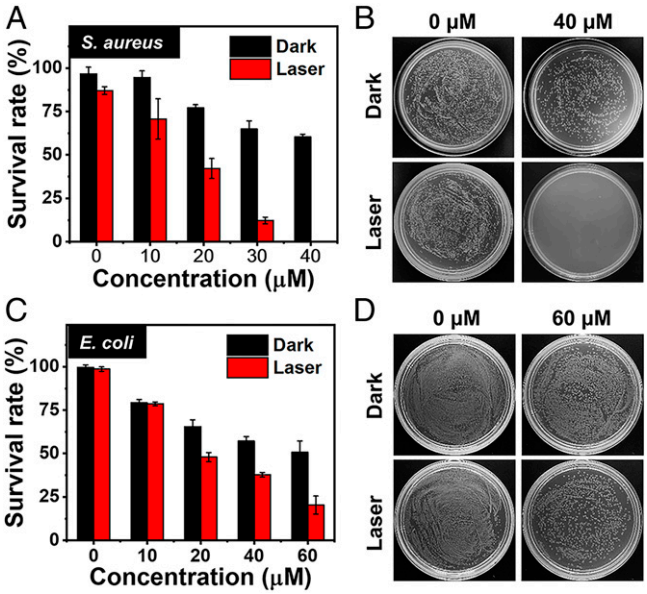

Fig. 3. Survival rate of (*A*) *Staphylococcus aureus* and (*C*) *Escherichia coli* were incubated with different concentrations of **1** in the dark or under 808-nm laser irradiation (0.8 W/cm^2). (*B* and *D*) Photographs of (*B*) *S. aureus* and (*D*) *E. coli* cultured on agar plates supplemented with different concentrations of **1** in the dark or under 808-nm laser irradiation (0.8 W/cm^2).

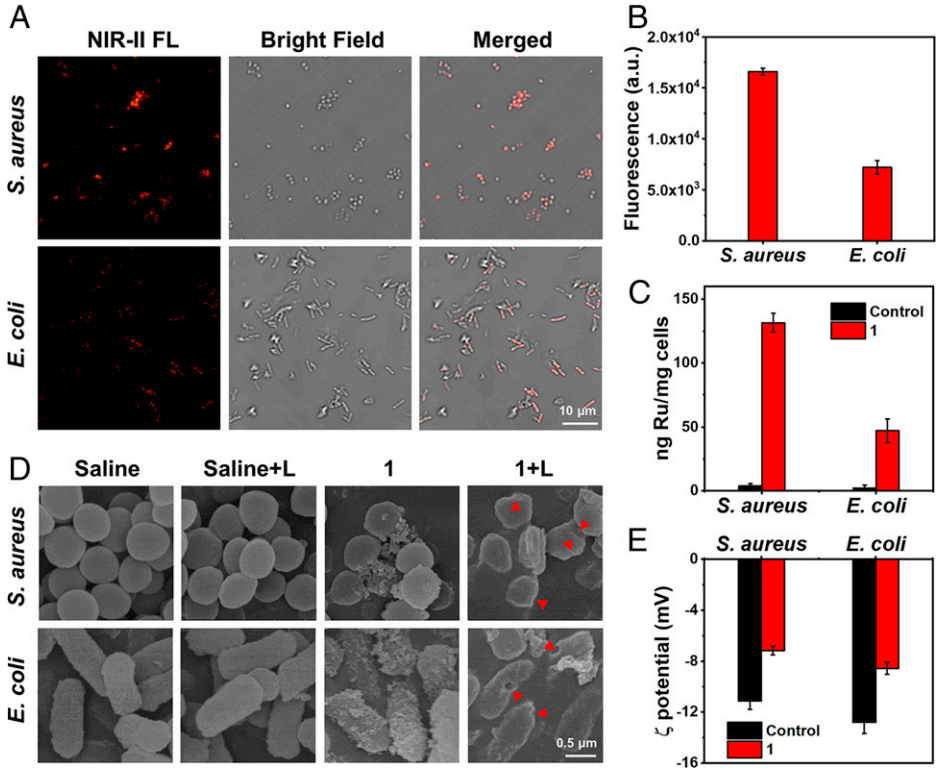

Fig. 4. (*A*) NIR-II fluorescent images of *Staphylococcus aureus* and *Escherichia coli* after being incubated with **1** for 2 h. Scale bar, 10 μm. (*B*) Fluorescent intensity of *S. aureus* and *E. coli* in *A*. (*C*) Inductively coupled plasma mass spectrometry result of Ru amount after *S. aureus* and *E. coli* incubation with **1** for 2 h. (*D*) Scanning electron microscope figures of *S. aureus* and *E. coli* after various treatments. Scale bar, 0.5 μm. (*E*) Zeta potential of *S. aureus* and *E. coli* in the presence or absence of **1**. a.u., arbitrary units; FL, fluorescence; L (as in "Saline+L"), laser.

lengthen the retention time in the blood circulation and accumulate more in the infection sites because the PEGylated NPs can escape the reticuloendothelial system (52, 53). The maximum absorption and emission wavelengths of NPs of **1** had no significant shift compared with **1** (*SI Appendix*, Fig. S28). Afterward, dynamic light-scattering results showed an average hydrodynamic diameter of ∼240 nm (*SI Appendix*, Fig. S29). The synthesized NPs of **1** exhibited high monodispersity and homogeneity, with an average particle size of ∼200 nm, as determined by transmission electron microscope (*SI Appendix*, Fig. S30). NPs of **1** also showed good size stability, as evidenced by the unchanged size distributions in phosphate-buffered saline and 10% fetal bovine serum over the course of 7 d in dynamic light-scattering studies (*SI Appendix*, Figs. S31 and S32). Besides, NPs of **1** exhibited chemical stability, photostability, and photothermal stability under different conditions, which facilitated further in vivo applications (*SI Appendix*, Figs. S33–S36). NPs of **1** also maintained good ROS-producing ability and photothermal properties compared with **1** (*SI Appendix*, Figs. S37 and S38). Finally, NPs of **1** did not induce noticeable hemolysis of red blood cells, thereby displaying good biocompatibility (*SI Appendix*, Figs. S39).

Afterward, we created the *S. aureus*–infected wound models in mice. NPs of **1** were administered to mice models by an intravenous injection. As illustrated in Fig. 5*A*, the fluorescent signal of the infected wound indicated the successful accumulation of NPs of **1** (54). Maximum accumulation of NPs of **1** was achieved after 24 h postinjection, with good values of signal-to-background ratio of ∼7.5 (Fig. 5*A* and *SI Appendix*, Figs. S40 and S41). The results of ex vivo biodistribution showed significant accumulation in infected skin and organs, including liver, spleen, and kidneys, rather than normal skin, indicating the specific accumulation in wound area after intravenous injection (*SI Appendix*, Figs. S42). The 24-h postinjection time was then selected as the optimal time point at which to perform phototherapy. Under the guidance of fluorescent imaging, we then assessed the effect of photo-triggered treatments (Fig. 5*B*). Recording the macroscopic appearance of the wound healing process at different time points over 6 d, the mice treated with NPs of **1** and subjected to laser photo-irradiation healed quickly, whereas the wounds in the control groups barely recovered (Fig. 5 *C* and *D*). The body weight of the mice was almost unchanged and hematoxylin and eosin–staining results verified no obvious adverse effects, indicating negligible histological toxicity (*SI Appendix*, Figs. S43 and S44). Hematoxylin and eosin–staining of infected skin slices provided further support of the improved healing effect on infected wounds with the combination of NPs of **1** and 808-nm laser photo-illumination (*SI Appendix*, Fig. S45).

Conclusion

We successfully constructed Ru (II) metallacycle **1** with an emissive wavelength beyond ∼1,000 nm. Metallacycle **1** exhibited superior optical penetration (∼7 mm) and effective antibacterial capability. In addition, **1** also showed promise of broad-spectrum antibacterial activity and had low toxicity to mammalian cells. After being prepared in NPs, **1** was employed in precise bacterial diagnosis and effective phototherapy in *S. aureus*–infected mice by NIR-II fluorescent imaging–guided photo-induced treatments. In this study, we developed an effective strategy to construct long-wavelength absorbing and emitting SCCs for both diagnostic and therapeutic applications.

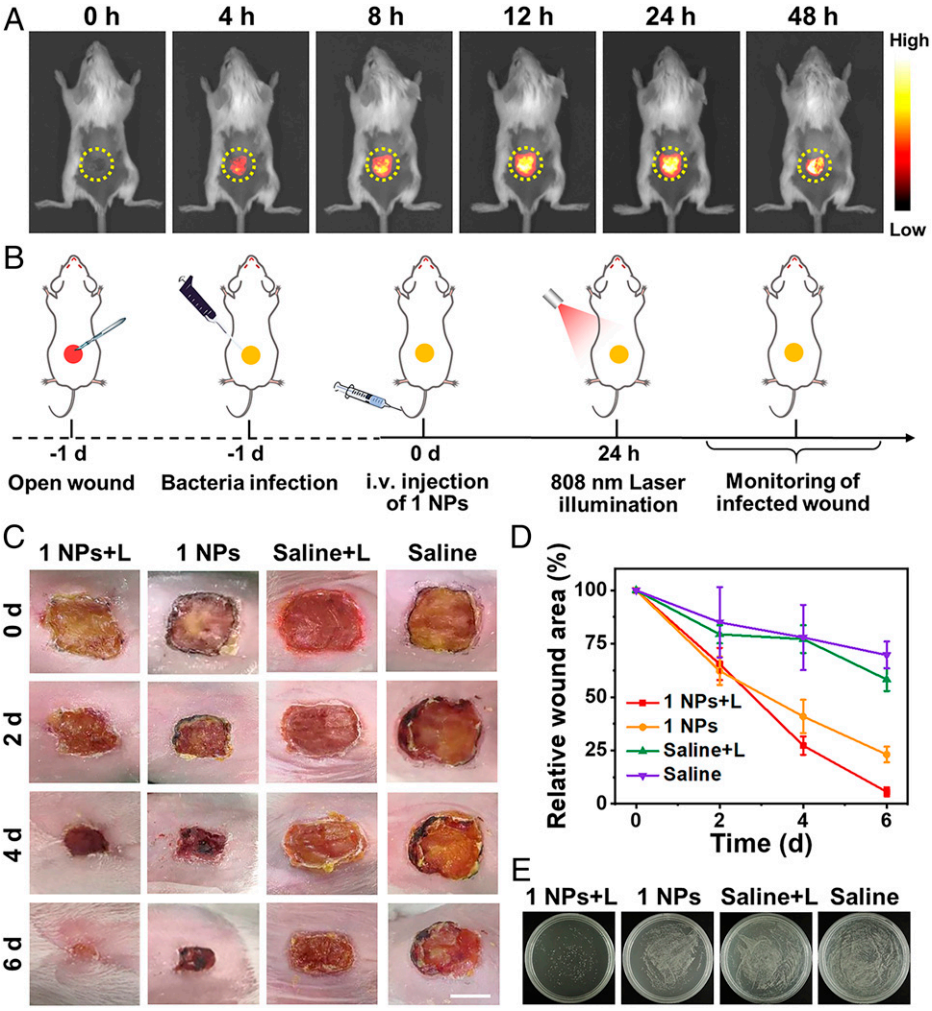

Fig. 5. (*A*) In vivo NIR-II fluorescent imaging of *Staphylococcus aureus*–infected wound models after intravenous (i.v.) injection of NPs of **1**. (*B*) Schematic illustration of treatment protocol for mice. (*C*) The photographs recording the infected wound and (*D*) the percentage of wound area change after various treatments. Scale bar, 5 mm. (*E*) Bacteria colonies formed by the *S. aureus* from wound area at 6 d postinjection. L (as in "Saline+L"), laser.

Materials and Methods

Mass spectra was tested in a Waters Synapt G2 tandem mass spectrometer. Fluorescent spectra were measured by a LS55 fluorescent spectrometer (PerkinElmer) using a quartz cuvette (Hellma). In vitro bacteria imaging and in vivo mice imaging were carried out with an NIR-II fluorescent microscope and an in vivo imaging system, respectively (Suzhou NIR-Optics). The 3-(4,5-dimethylthiazol-2-yl)-2,5-diphenyl-2H-tetrazolium bromide (MTT) assay was analyzed by a microplate reader (Epoch 2; BioTek) using a 96-well microplate (Nest). All animal experiments were performed under the guidelines of the Institutional Animal Care and Use Committee of Central China Normal University.

Data Availability. All study data are included in the article and/or supporting information. Data were available from the corresponding authors upon request.

ACKNOWLEDGMENTS. This work was supported by National Natural Science Foundation of China (Grants 22022404 and 22074050), the open research fund supported by the Ministry of Education Key Laboratory for the Synthesis and Application of Organic Functional Molecules Hubei University (No. KLSAOFM2111), the Fundamental Research Funds for the Central Universities (CCNU20QN007) and the Open Project Program of Guangxi Key Laboratory of Brain and Cognitive Neuroscience, Guilin Medical University (GKLBCN-202106-01, to Yao Sun).

Author affiliations: [a]Key Laboratory of Pesticides and Chemical Biology, Ministry of Education, International Joint Research Center for Intelligent Biosensor Technology and Health, College of Chemistry, Central China Normal University, Wuhan 430079, China; [b]Department of Chemistry, University of Utah, Salt Lake City, UT 84112; [c]Ministry of Education Key Laboratory for the Synthesis and Application of Organic Functional Molecular, College of Chemistry and Chemical Engineering, Hubei University, Wuhan 430062, China; [d]College of Chemistry and Environmental Engineering, Shenzhen University, Shenzhen, Guangdong 518060, China; and [e]Ministry of Education Key Laboratory for Special Functional Materials, Henan University, Kaifeng 475004, China

1. S. E. Rossiter, M. H. Fletcher, W. M. Wuest, Natural products as platforms to overcome antibiotic resistance. *Chem. Rev.* **117**, 12415–12474 (2017).
2. D. L. Heymann, Resistance to anti-infective drugs and the threat to public health. *Cell* **124**, 671–675 (2006).
3. C. M. Moore, D. Pendse, M. Emberton, Photodynamic therapy for prostate cancer–A review of current status and future promise. *Nat. Clin. Pract. Urol.* **6**, 18–30 (2009).
4. J. P. Celli *et al.*, Imaging and photodynamic therapy: Mechanisms, monitoring, and optimization. *Chem. Rev.* **110**, 2795–2838 (2010).
5. T. C. Pham, V. N. Nguyen, Y. Choi, S. Lee, J. Yoon, Recent strategies to develop innovative photosensitizers for enhanced photodynamic therapy. *Chem. Rev.* **121**, 13454–13619 (2021).
6. J. Liu *et al.*, Harnessing ruthenium(II) as photodynamic agents: Encouraging advances in cancer therapy. *Coord. Chem. Rev.* **363**, 17–28 (2018).
7. M. Kang *et al.*, Evaluation of structure-function relationships of aggregation-induced emission luminogens for simultaneous dual applications of specific discrimination and efficient photodynamic killing of gram-positive bacteria. *J. Am. Chem. Soc.* **141**, 16781–16789 (2019).
8. D. Mao *et al.*, Metal-organic-framework-assisted in vivo bacterial metabolic labeling and precise antibacterial therapy. *Adv. Mater.* **30**, e1706831 (2018).
9. E. D. Anderson, A. P. Gorka, M. J. Schnermann, Near-infrared uncaging or photosensitizing dictated by oxygen tension. *Nat. Commun.* **7**, 13378 (2016).
10. S. Monro *et al.*, Transition metal complexes and photodynamic therapy from a tumor-centered approach: Challenges, opportunities, and highlights from the development of TLD1433. *Chem. Rev.* **119**, 797–828 (2019).
11. A. Notaro, G. Gasser, Monomeric and dimeric coordinatively saturated and substitutionally inert Ru(II) polypyridyl complexes as anticancer drug candidates. *Chem. Soc. Rev.* **46**, 7317–7337 (2017).

12. Y. Xu *et al.*, NIR-II emissive multifunctional AIEgen with single laser-activated synergistic photodynamic/photothermal therapy of cancers and pathogens. *Biomaterials* **259**, 120315 (2020).
13. X. Zhao, J. Liu, J. Fan, H. Chao, X. Peng, Recent progress in photosensitizers for overcoming the challenges of photodynamic therapy: From molecular design to application. *Chem. Soc. Rev.* **50**, 4185–4219 (2021).
14. F. Heinemann, J. Karges, G. Gasser, Critical overview of the use of Ru(II) polypyridyl complexes as photosensitizers in one-photon and two-photon photodynamic therapy. *Acc. Chem. Res.* **50**, 2727–2736 (2017).
15. A. Raza *et al.*, A dinuclear ruthenium(II) complex excited by near-infrared light through two-photon absorption induces phototoxicity deep within hypoxic regions of melanoma cancer spheroids. *J. Am. Chem. Soc.* **142**, 4639–4647 (2020).
16. J. Karges *et al.*, Rationally designed long-wavelength absorbing Ru(II) polypyridyl complexes as photosensitizers for photodynamic therapy. *J. Am. Chem. Soc.* **142**, 6578–6587 (2020).
17. S. Angerani, N. Winssinger, Visible light photoredox catalysis using ruthenium complexes in chemical biology. *Chemistry* **25**, 6661–6672 (2019).
18. W. Tuo *et al.*, Biomedical applications of Pt(II) metallacycle/metallacage-based agents: From mono-chemotherapy to versatile imaging contrasts and theranostic platforms. *Coord. Chem. Rev.* **443**, 214017 (2021).
19. Y. Sun, C. Chen, J. Liu, P. J. Stang, Recent developments in the construction and applications of platinum-based metallacycles and metallacages via coordination. *Chem. Soc. Rev.* **49**, 3889–3919 (2020).
20. Y. Sun *et al.*, Melanin-dot-mediated delivery of metallacycle for NIR-II/photoacoustic dual-modal imaging-guided chemo-photothermal synergistic therapy. *Proc. Natl. Acad. Sci. U.S.A.* **116**, 16729–16735 (2019).
21. Z. Zhou *et al.*, A self-assembled Ru-Pt metallacage as a lysosome-targeting photosensitizer for 2-photon photodynamic therapy. *Proc. Natl. Acad. Sci. U.S.A.* **116**, 20296–20302 (2019).
22. J. Zhou, G. Yu, F. Huang, Supramolecular chemotherapy based on host-guest molecular recognition: A novel strategy in the battle against cancer with a bright future. *Chem. Soc. Rev.* **46**, 7021–7053 (2017).
23. Y. Qin, X. Liu, P. P. Jia, L. Xu, H. B. Yang, BODIPY-based macrocycles. *Chem. Soc. Rev.* **49**, 5678–5703 (2020).
24. S. Bhattacharyya *et al.*, Self-assembled Pd_{12} coordination cage as photoregulated oxidase-like nanozyme. *J. Am. Chem. Soc.* **142**, 18981–18989 (2020).
25. O. Domarco *et al.*, Subcellular duplex DNA and G-quadruplex interaction profiling of a hexagonal Pt^{II} metallacycle. *Angew. Chem. Int. Ed. Engl.* **58**, 8007–8012 (2019).
26. H. Sepehrpour, W. Fu, Y. Sun, P. J. Stang, Biomedically relevant self-assembled metallacycles and metallacages. *J. Am. Chem. Soc.* **141**, 14005–14020 (2019).
27. Y. Sun *et al.*, Self-assembly of metallacages into centimeter films with tunable size and emissions. *J. Am. Chem. Soc.* **142**, 17933–17937 (2020).
28. X. Yan, T. R. Cook, P. Wang, F. Huang, P. J. Stang, Highly emissive platinum(II) metallacages. *Nat. Chem.* **7**, 342–348 (2015).
29. J. Zhou *et al.*, Highly emissive self-assembled BODIPY-platinum supramolecular triangles. *J. Am. Chem. Soc.* **140**, 7730–7736 (2018).
30. P. P. Jia *et al.*, Orthogonal self-assembly of a two-step fluorescent-resonance energy transfer system with improved photosensitization efficiency and photooxidation activity. *J. Am. Chem. Soc.* **143**, 399–408 (2021).
31. S. Gao *et al.*, Membrane intercalation-enhanced photodynamic inactivation of bacteria by a metallacycle and TAT-decorated virus coat protein. *Proc. Natl. Acad. Sci. U.S.A.* **116**, 23437–23443 (2019).
32. H. Wang *et al.*, Assembling pentatopic terpyridine ligands with three types of coordination moieties into a giant supramolecular hexagonal prism: Synthesis, self-assembly, characterization, and antimicrobial study. *J. Am. Chem. Soc.* **141**, 16108–16116 (2019).
33. P. Jeyakkumar *et al.*, Emissive metallacycle-crosslinked supramolecular networks with tunable crosslinking densities for bacterial imaging and killing. *Angew. Chem. Int. Ed. Engl.* **59**, 15199–15203 (2020).
34. Y. Xu *et al.*, Design of a metallacycle-based supramolecular photosensitizer for in vivo image-guided photodynamic inactivation of bacteria. *Angew. Chem. Int. Ed. Engl.* **61**, e202110048 (2022).
35. Y. Sun *et al.*, Rhomboidal Pt(II) metallacycle-based NIR-II theranostic nanoprobe for tumor diagnosis and image-guided therapy. *Proc. Natl. Acad. Sci. U.S.A.* **116**, 1968–1973 (2019).
36. J. L. Zhu *et al.*, Switchable organoplatinum metallacycles with high quantum yields and tunable fluorescence wavelengths. *Nat. Commun.* **10**, 4285 (2019).
37. S. Li *et al.*, Design of a tris-heteroleptic Ru(II) complex with red-light excitation and remarkably improved photobiological activity. *Inorg. Chem.* **59**, 11193–11204 (2020).
38. J. Wang *et al.*, Self-assembled manganese phthalocyanine nanoparticles with enhanced peroxidase-like activity for anti-tumor therapy. *Nano Res.* **15**, 2347–2354 (2022).
39. J. Li *et al.*, Recent advances in the development of NIR-II organic emitters for biomedicine. *Coord. Chem. Rev.* **415**, 213318 (2020).
40. G. Hong, A. L. Antaris, H. Dai, Near-infrared fluorophores for biomedical imaging. *Nat. Biomed. Eng.* **1**, 0010 (2017).
41. C. Xu, K. Pu, Second near-infrared photothermal materials for combinational nanotheranostics. *Chem. Soc. Rev.* **50**, 1111–1137 (2021).
42. S. He, J. Song, J. Qu, Z. Cheng, Crucial breakthrough of second near-infrared biological window fluorophores: Design and synthesis toward multimodal imaging and theranostics. *Chem. Soc. Rev.* **47**, 4258–4278 (2018).
43. Y. Liu *et al.*, Versatile types of inorganic/organic NIR-IIa/IIb fluorophores: From strategic design toward molecular imaging and theranostics. *Chem. Rev.* **122**, 209–268 (2022).
44. Y. Fan *et al.*, Lifetime-engineered NIR-II nanoparticles unlock multiplexed in vivo imaging. *Nat. Nanotechnol.* **13**, 941–946 (2018).
45. C. Li, G. Chen, Y. Zhang, F. Wu, Q. Wang, Advanced fluorescent imaging technology in the near-infrared-II window for biomedical applications. *J. Am. Chem. Soc.* **142**, 14789–14804 (2020).
46. C. Li *et al.*, Rationally designed Ru(II)-metallacycle chemo-phototheranostic that emits beyond 1000 nm. *Chem. Sci. (Camb.)* **13**, 6541–6549 (2022).
47. Y. Xu *et al.*, Construction of emissive ruthenium(II) metallacycle over 1000 nm wavelength for in vivo biomedical applications. *Nat. Commun.* **13**, 2009 (2022).
48. Y. Zhao *et al.*, Self-assembled ruthenium (II) metallacycles and metallacages with imidazole-based ligands and their in vitro anticancer activity. *Proc. Natl. Acad. Sci. U.S.A.* **116**, 4090–4098 (2019).
49. M. L. Saha, X. Yan, P. J. Stang, Photophysical properties of organoplatinum(II) compounds and derived self-assembled metallacycles and metallacages: Fluorescent and its applications. *Acc. Chem. Res.* **49**, 2527–2539 (2016).
50. Z. Sheng *et al.*, Smart human serum albumin-indocyanine green nanoparticles generated by programmed assembly for dual-modal imaging-guided cancer synergistic phototherapy. *ACS Nano* **8**, 12310–12322 (2014).
51. T. Wu *et al.*, Identification of a protein complex that assembles lipopolysaccharide in the outer membrane of *Escherichia coli*. *Proc. Natl. Acad. Sci. U.S.A.* **103**, 11754–11759 (2006).
52. S. Dadashzadeh, A. M. Vali, M. Rezaie, The effect of PEG coating on in vitro cytotoxicity and in vivo disposition of topotecan loaded liposomes in rats. *Int. J. Pharm.* **353**, 251–259 (2008).
53. J. S. Suk, Q. Xu, N. Kim, J. Hanes, L. M. Ensign, PEGylation as a strategy for improving nanoparticle-based drug and gene delivery. *Adv. Drug Deliv. Rev.* **99** (Pt A), 28–51 (2016).
54. T. Lian, R. J. Y. Ho, Trends and developments in liposome drug delivery systems. *J. Pharm. Sci.* **90**, 667–680 (2001).